ELSEVIER

Chemical Engineering Journal 136 (2008) 383–389

Chemical Engineering Journal

www.elsevier.com/locate/cej

Physical and electrical properties of Zr–Cu substituted strontium hexaferrite nanoparticles synthesized by co-precipitation method

Muhammad Javed Iqbal *, Muhammad Naeem Ashiq

Surface and Solid State Chemistry Laboratory, Department of Chemistry, Quaid-i-Azam University, Islamabad 45320, Pakistan

Received 7 February 2007; received in revised form 10 May 2007; accepted 21 May 2007

Abstract

The magnetic and electrical behavior of $SrZr_xCu_xFe_{12-2x}O_{19}$ (where $x = 0.0$–0.8) hexaferrite nanoparticles are reported in this paper. Five samples were synthesized by the chemical co-precipitation method. $SrFe_{12}O_{19}$ is a semiconductor however doping Zr_xCu_x at iron sites resulted in a semiconductor-metal transition at a temperature $T_{M–S}$. The structural parameters of the samples were obtained by FTIR, XRD, EDX, SEM and TEM analyses. The FTIR spectrum and XRD pattern of the samples showed that the synthesized materials were of a single phase. The particle size was in the range 26–37 nm as estimated by Scherrer formula, which is comparable with the values estimated from SEM (40–80 nm) and TEM (30–60 nm) analyses. AC magnetic susceptibility and DC electrical resistivity measurements were carried out in a temperature range 300–800 K. The Curie temperature (T_C) decreases on substitution of Zr–Cu. A significant increase in the room temperature resistivity is noted with the addition of Zr–Cu up to $x \leq 0.4$. The drift mobility (μ_d) and the activation energy (ΔE) are also calculated from electrical resistivity data. The variation of the dielectric constant (ε') and the dielectric loss factor ($\tan \delta$) with frequency in the range 80 Hz–1 MHz and composition of the sample is observed.

Keywords: Strontium hexaferrite; Nanoparticles; Metal-semiconductor transition; DC electrical resistivity; Dielectric constant

1. Introduction

Nanomaterials represent a novel class of materials in which a significant fraction of atoms is present on the surface that induces properties distinctly different from those of the normal polycrystalline materials [1,2]. Very recently, attention has been drawn towards nano-crystalline ferrites because of their wide applications in industry and technology [3]. Strontium hexaferrite is considered a material with promising scientific and technological applications in the fields of telecommunication, data recording and microwave devices etc. Also, it has relatively high values of magnetic anisotropy, electrical resistivity and Curie temperature in addition to possessing excellent chemical stability and corrosion resistivity [4,5]. For the preparation of hexaferrite, the solid-state reaction method [6] is commonly employed that involves firing of a stoichiometric mixture of Sr-carbonate and α-Fe_2O_3 at high temperature ($\sim$1200 °C) but obtaining ultra fine and mono dispersed particles may not be easy. Several low-temperature methods, namely, sol–gel [7], aerosol pyrolysis [8], glass crystallization [9], microemulsion [10], sonochemical [11] and hydrothermal [12] techniques have also been suggested. However, some of these methods are complex and may require expensive equipment. The chemical co-precipitation method [13] ensures proper distribution of various metal ions resulting into stoichiometric and smaller particles size product compared to some of the others. For instance, Sr-hexaferrite samples prepared by the coprecipitation method are much smaller in size (26–37 nm) as compared to those prepared by sol–gel method (90–110 nm) [7] and by glass crystallization method (50–330 nm) [9].

Several cations, such as Cr^{3+}, Al^{3+}, Ga^{3+}, In^{3+} and cation combinations such as La^{3+}–Co^{2+}, Gd^{3+}–Co^{2+}, Nb^{4+}–Zn^{2+}, Ir^{4+}–Zn^{2+}, Sm^{3+}–Co^{2+}, Ti^{4+}–Mn^{2+}, Ti^{4+}–Ni^{2+} and Ti^{4+}–Co^{2+} have been attempted by several researchers [14–19] in order to improve the properties of Sr-hexaferrite. Popularly, Ti^{4+}–Co^{2+} combination substituted at iron site in M-type hexaferrites is known to be effective in reducing the magnetocrystalline anisotropy and enhancing the electrical resistivity; the properties suitable for a wide range of industrial applications. However, Ti^{4+}–Co^{2+} substituted hexaferrite requires costly titanium salts for chemical synthesis and also needs heat treatment at high temperatures. For the application in microwave devices high elec-

* Corresponding author. Tel.: +92 51 9219811; fax: +92 51 2873869.
E-mail address: mjiqauchem@yahoo.com (M.J. Iqbal).

1385-8947/$ – see front matter © 2007 Elsevier B.V. All rights reserved.
doi:10.1016/j.cej.2007.05.046

trical resistivity material is more suitable [20]. The substitution of Cu may be helpful in influencing the permeability, magnetic susceptibility and electrical resistivity [21]. In the present study, titanium is replaced by zirconium because it is isoelectronic with Ti^{4+} and its salts are less costly. It is also possible that a combination of Cu^{2+} with Zr^{4+} can improve the dielectric constant and electrical resistivity without affecting phase formation.

We have used a chemical co-precipitation method [13] to synthesis Zr–Cu substituted strontium hexaferrite $SrZr_xCu_xFe_{12-2x}O_{19}$ samples with $x = 0.0$–0.8. The unit cell volumes (V), X- ray density (ρ_x), bulk density (ρ_m), porosity (P), metal-semiconductor transition temperature (T_{M-S}), the Curie temperature (T_C), drift mobility (μ_d), activation energy (ΔE) in a temperature range 300–700 K, dielectric constant (ε') and the dielectric loss factor (tan δ) in frequency range 80 Hz–1 MHz are reported in this paper.

2. Materials and method

2.1. Sample preparation

The chemicals used in the synthesis of samples were $Fe(NO_3)_3{\cdot}9H_2O$ (Panreac Quimica SA, 98%), $Sr(NO_3)_2$ (Fluka, ≥99%), $Cu(CH_3COO)_2{\cdot}H_2O$ (Merck, 99%), $ZrOCl_2{\cdot}4H_2O$ (BDH, 96%) and NaOH (Fluka, ≥97%). The strontium hexaferrite samples substituted with Zr–Cu and having nominal composition $SrZr_xCu_xFe_{12-2x}O_{19}$ (where $x = 0.0$–0.8) were prepared by a chemical coprecipitation method [13] maintaining the Fe/Sr molar ratio of 11. The 2 M solution of NaOH was used as precipitating agent. The precipitates were washed with distilled water, dried at 100 °C in an oven. Pellets of 13 mm diameter and 3 mm thickness were obtained under 90 kN pressure and annealed at an optimized temperature 920 °C for 1 h in a temperature programmed tube furnace (Carbolite CTF 12/100) at a heating rate of 5 °C/min.

The infra red spectrum of a sample ($SrZr_{0.4}Cu_{0.4}Fe_{11.2}O_{19}$) was recorded by FTIR spectrophotometer (Bio Rad Merlin FTS3000MX) showing absorption bands at 592, 557 and 439 cm^{-1} identified as the metal oxygen stretching vibrations of hexaferrite [22]. The absence of any additional peaks confirms a single hexaferrite phase.

Perkin Elmer (TGA-7) thermogravimetric analyzer with computer interface was employed to investigate the changes that occur on heating the sample at heating rate of 10 °C/min. Thermogravimetric curve for an unannealed sample ($SrFe_{12}O_{19}$) shows weight losses at 135.9, 316.5, 529.9 and 702.0 °C (Fig. 1). The loss at 135.9 °C is due to loss of water and that at 316.5 °C is due to the decomposition of hydroxide into oxide. The loss at 529.9 and 702.0 °C is attributed to the formation of strontium monoferrite ($SrO{\cdot}Fe_2O_3$) and strontium hexaferrite ($SrO{\cdot}6Fe_2O_3$), respectively. The TG analysis indicates that the strontium hexaferrite can be formed at a relatively low temperature of 702 °C compared to 780 °C for its synthesis by the sol–gel method [23]. The $SrO{\cdot}Fe_2O_3$ phase however is also converted into a single $SrFe_{12}O_{19}$ phase on annealing as evidenced by both FTIR and XRD results. The reaction scheme for the coprecipitation method is described as follows:

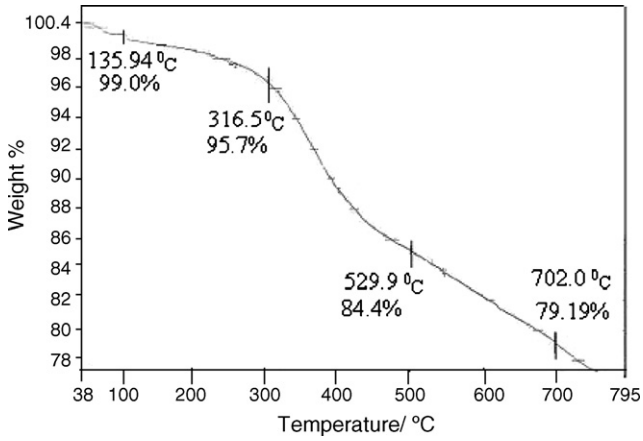

Fig. 1. TGA curve for un-annealed sample of strontium hexaferrite.

$$2Sr(NO_3)_2(aq) + 4Fe(NO_3)_3(aq) + 16NaOH(aq) \rightarrow Sr_2Fe_4(OH)_{16}.nH_2O + 16\,NaNO_3(aq)$$

$$\downarrow 316.5^{\circ}C$$

$$SrFe_{12}O_{19} \xleftarrow{920^{\circ}C} SrO + SrO.Fe_2O_3 + Fe_2O_3 + 8H_2O$$

The results of quantitative EDX elemental analysis of $SrZr_xCu_xFe_{12-2x}O_{19}$ ($x = 0.0$–0.8) samples using Oxford Inca-200 EDX analyzer are in excellent agreement with its nominal composition as shown in Table 1. The molar ratio of strontium (Sr) was kept slightly higher, i.e. 1.1, in these samples because the solubility of Fe is higher as compared to strontium. A single hexagonal phase was found when Fe/Sr = 11 whereas the samples, in which the Fe/Sr molar ratio of 12 was maintained, an additional nonmagnetic α-Fe_2O_3 phase also appeared along with hexagonal phase.

The SEM images of samples containing Zr–Cu ($x = 0.0$, 0.4 and 0.8) were recorded by Jeol JSM 5910 microscope. They clearly show that the surface is less smooth for sample with $x = 0.0$ and 0.4 and also has some shaded areas due to voids (Fig. 2a and b). The white spots show that the material is not homogeneous but as the substitution is increased the material

Table 1
The elemental composition of $SrZr_xCu_xFe_{12-2x}O_{19}$ samples as determined by EDX analysis

Elements	$x = 0.00$	$x = 0.2$	$x = 0.4$	$x = 0.6$	$x = 0.8$
Sr	1.10	1.08	1.05	1.10	1.06
Fe	11.93	11.51	11.14	10.72	10.30
Zr	–	0.18	0.39	0.62	0.81
Cu	–	0.21	0.43	0.56	0.75

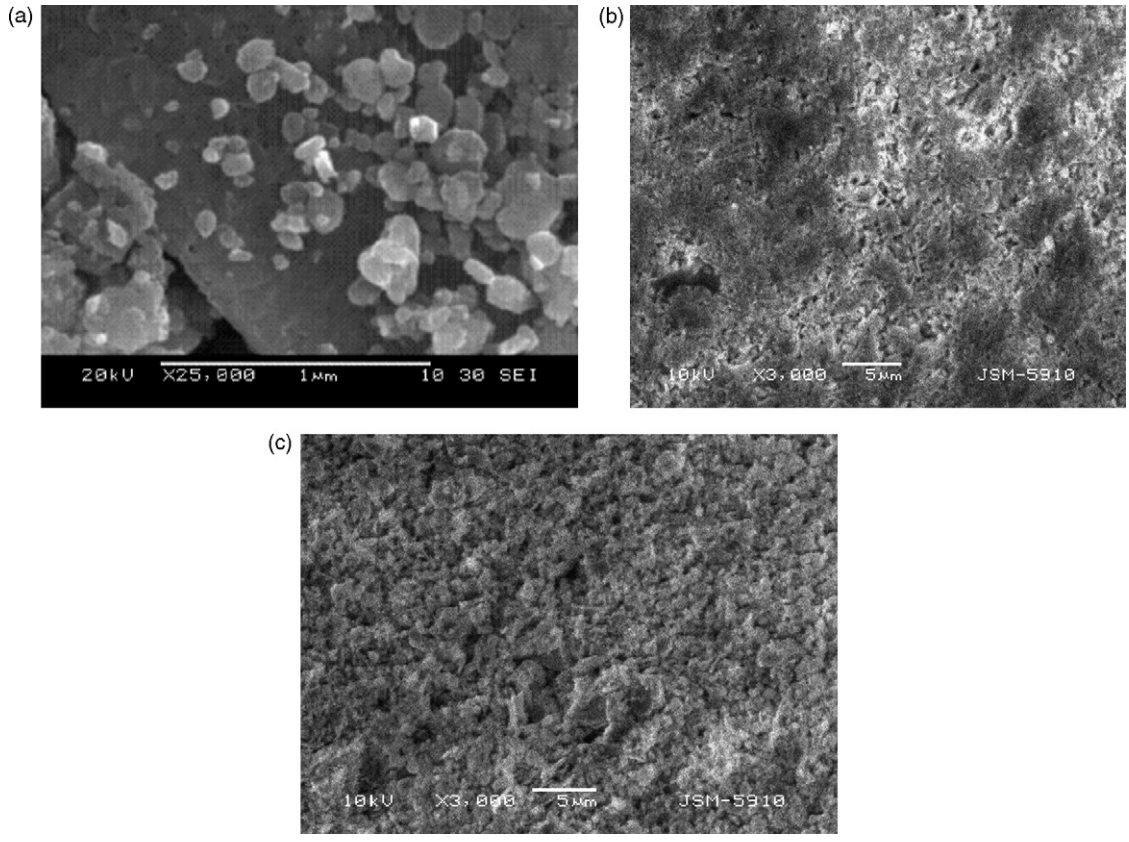

Fig. 2. Scanning electron microscopy (SEM) photographs of (a) $x = 0.0$, (b) $x = 0.4$ and (c) $x = 0.8$.

becomes homogeneous and monodispersed. The sample with $x = 0.8$, the surface becomes smoother and the number of voids also decrease and it can be noted that the particles have well defined shape and clear boundaries. Furthermore, the surface of the latter sample appears to be more compact (Fig. 2c). The particle sizes calculated from SEM and TEM (not shown) of the unsubstituted sample were found 40–80 nm and 30–60 nm, respectively, and have been compared with those estimated by the Scherrer formula (26–37 nm).

Powder XRD analysis was performed by Philips X'Pert PRO 3040/60 diffractometer, which uses CuK_α as a radiation source. The AC magnetic susceptibility was measured using a primary and secondary coil set up operating at a frequency of 273 Hz, and a very low AC field (0.1 Oe) was applied parallel to the axis of a disc shaped sample as described elsewhere [24]. The DC electrical resistivity was measured by a two-point probe method described previously [25]. The dielectric measurements were carried out at room temperature in a frequency range 80 Hz–1 MHz using a LCR meter bridge (Wayne Kerr LCR 4275).

3. Results and discussion

3.1. X-ray diffraction analysis

The powder XRD patterns of annealed $SrZr_xCu_xFe_{12-2x}O_{19}$ samples with $x = 0.0$–0.8 are shown in Fig. 3. Clearly, all of these possess a magnetoplumbite single phase. The lattice parameters 'a' and 'c' show that the values of 'a' remain almost constant but the values of 'c' increase by increasing the Zr–Cu content, x, as shown in Table 2. This is attributed to larger ionic radii of the dopants viz. Cu^{2+} (0.73 Å) and Zr^{4+} (0.80 Å) than that of Fe^{3+} (0.64 Å). The XRD data are used to estimate the unit cell volume (V) and the X- ray density (ρ_x) of the samples. The bulk density (ρ_m) and porosity (P) of the samples are also calculated. The following relations are used for obtaining the values of the parameters listed in Table 2.

$$V = 0.8666\, a^2 c \tag{1}$$

$$\rho_x = \frac{2M}{NV} \tag{2}$$

$$\rho_m = \frac{m}{\pi r^2 h} \tag{3}$$

$$P = 1 - \frac{\rho_m}{\rho_x} \tag{4}$$

where m is the mass; M, the molar mass of the sample; N, the Avogadro's number; r, the radius; and h is the height (thickness) of the pellet.

The value of the X-ray density increases on increasing the Zr–Cu content of the samples, which is considered to be due to larger sizes of Zr and Cu compared to that of Fe as discussed above. Table 2 shows that the value of ρ_m is smaller than that of the value of ρ_x. This is attributed to the existence of pores in the samples. The values of porosity, P, decrease with the substitution of Zr–Cu content reaching a minima at $x = 0.4$. The crystallite

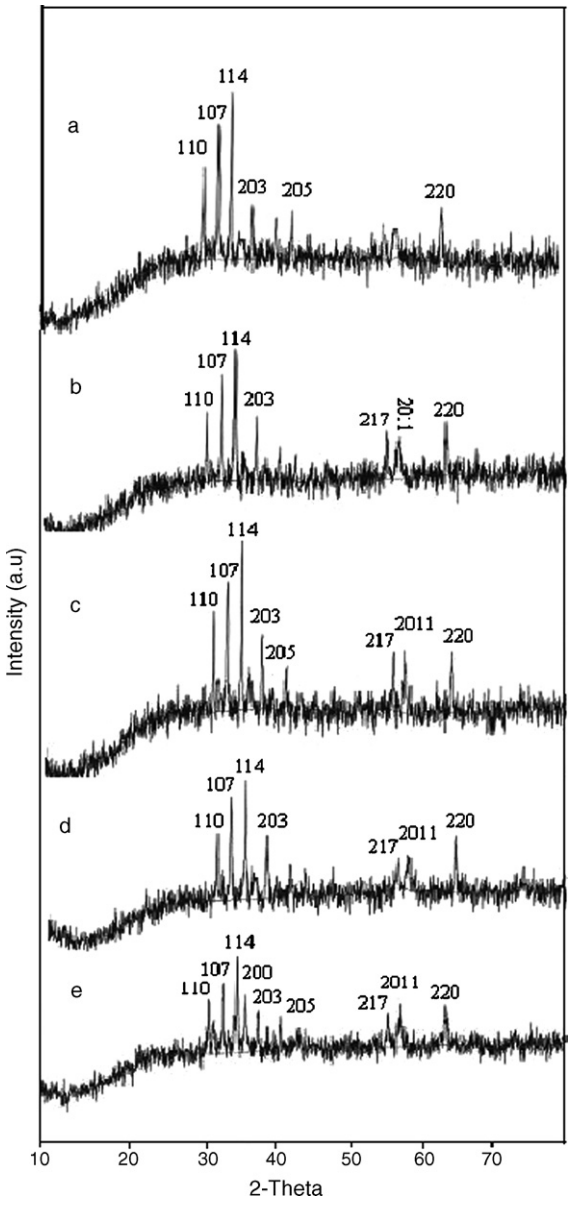

Fig. 3. Indexed X-ray diffraction pattern of $SrZr_xCu_xFe_{12-x}O_{19}$ nanoparticles $a = (x = 0.0)$, $b = (x = 0.2)$, $c = (x = 0.4)$, $d = (x = 0.6)$ and $e = (0.8)$.

size (D) of the samples in the range 26–37 nm is calculated by the Scherrer formula (Table 2), 40–80 nm by SEM and 30–60 nm by TEM analyses which are much smaller than 4.69 μm for the barium hexaferrites also prepared by the co-precipitation method by Shepherd et al. [20].

3.2. Magnetic susceptibility measurements

Measurement of temperature dependence of magnetic susceptibility is considered to be a suitable method for the analysis of various kinds of magnetic materials because this technique is more sensitive to low impurity content than the Mössbaur or XRD diffraction methods [26]. Fig. 4 shows the AC magnetic susceptibility plotted as a function of temperature for different samples of $SrZr_xCu_xFe_{12-2x}O_{19}$ ($x = 0.0$–0.8). A sharp peak near the Curie temperature T_C indicates the presence of a pure phase

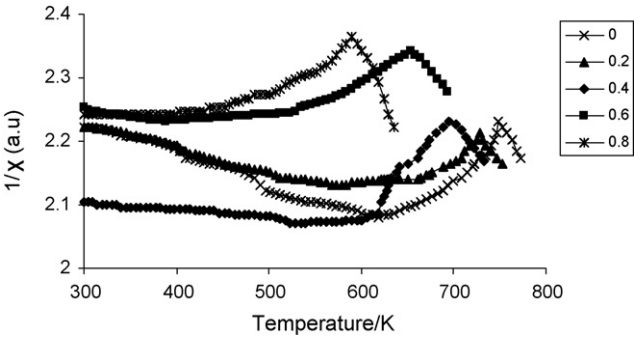

Fig. 4. Temperature dependence of the inverse of susceptibility of different $SrZr_xCu_xFe_{12-2x}O_{19}$ ($x = 0.0$–0.8) hexaferrite samples.

in the samples. It can be noted that the T_C decreases as the Zr–Cu content (x) is increased (Table 2). The substitution of Zr^{4+}, a non magnetic ion, and Cu^{2+}, having lower value of magnetic moment (1 μB) than Fe^{3+} (5 μB), is believed to be causing a weakening of the superexchange interactions between Fe^{3+} and O^{2-} ions.

3.3. Resistivity measurements

The undoped $SrFe_{12}O_{19}$ sample is a semiconductor throughout the temperature range studied i.e. 300–700 K. However, doping with Zr_xCu_x ($x = 0.2$–0.8) results in the semiconductor to metal transition. Similar transitions have also been observed in Al–Cr substituted nickel ferrites [27]. The doped samples exhibit a semiconductor behavior and the resistivity reaches a maximum value at the temperature, T_{M-S}, defined as metal–semiconductor transition temperature. The temperature dependence of DC electrical resistivity (ρ) of the samples is shown in Fig. 5. The T_{M-S} increases with the addition of dopant. Furthermore, the peak height of resistivity value increases corresponding to Zr_xCu_x contents up to $x \leq 0.4$ but sharply decreases for $x > 0.4$. The initial resistivity increase with the temperature is indicative of the metallic behavior and the following decrease in resistivity represents semiconductor.

According to the Rezlescu model [28], the conductivity in ferrites is due to the hopping of electrons between Fe^{3+} and Fe^{2+} at the octahedral sites. The value of room temperature resistivity is increased for the samples $x \leq 0.4$ due to replacement of Fe

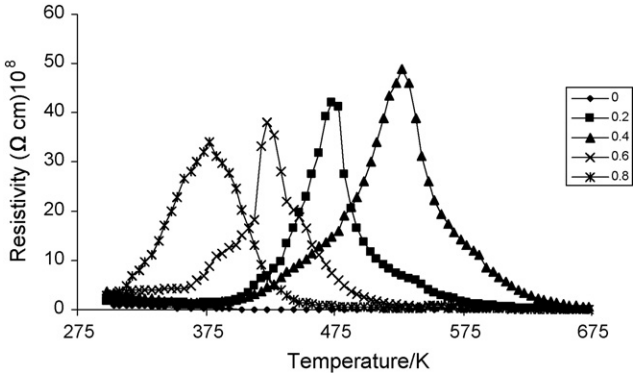

Fig. 5. Variation of electrical resistivity with temperature for different $SrZr_xCu_xFe_{12-2x}O_{19}$ ($x = 0.0$–0.8) hexaferrite samples.

Table 2
Crystallite size (D), lattice constants (a and c), cell volume (V), X-ray density (ρ_x), bulk density (ρ_m), porosity (P), Curie temperature (T_C), electrical resistivity (ρ), activation energy (ΔE), drift mobility (μ_d), dielectric constant (ε') and dielectric loss factor ($\tan\delta$) of $SrZr_xCu_xFe_{12-2x}O_{19}$

Parameters	$x=0.0$	$x=0.2$	$x=0.4$	$x=0.6$	$x=0.8$
Crystallites size (D, nm)	30	37	33	26	37
Lattice constant (a, Å)	5.87	5.88	5.88	5.88	5.87
Lattice constant (c, Å)	23.06	23.16	23.17	23.20	23.21
Cell volume (V, Å^3)	688	693	694	695	693
X-ray density (ρ_x, g/cm^3)	5.12	5.13	5.16	5.20	5.26
Bulk density (ρ_m, g/cm^3)	2.36	3.15	3.47	3.45	3.24
Porosity (P, %)	0.54	0.39	0.33	0.34	0.38
Curie temperature (T_C, °C)	475	457	423	381	316
Resistivity (ρ, 10^8 Ω cm at 298 K)	0.89	1.63	3.71	2.91	2.21
Activation energy (ΔE, eV)	0.74	0.86	0.95	0.71	0.50
Drift mobility (μ_d, 10^{-13} cm^2/V/s at 298 K)	28.68	17.88	8.04	10.86	14.69
Dielectric constant (ε' at 400 kHz)	252	218	133	183	230
Dielectric constant (ε' at 600 KHz)	221	187	121	163	196
Dielectric constant (ε' at 1 MHz)	183	145	110	154	163
Dielectric loss factor ($\tan\delta$ at 600 KHz)	1.260	0.979	0.564	1.465	2.017
Dielectric loss factor ($\tan\delta$ at 1 MHz)	0.983	0.848	0.496	1.081	1.548

ions from octahedral sites by the substitution of Cu ions. This reduces the number of Fe ions at octahedral sites, which results in decrease of electron hopping and the number of Fe^{2+} ions thus causing the resistivity to increase. The Cu^{2+} ion occupies the lattice interstitial octahedral B site and distorts the lattice to generate internal stress, which confines the electron hopping and then reduces the Fe^{2+} generation [29]. Zr^{4+} ion has a preference for the trigonal bipyramidal and tetrahedral site [30] but owing to its small concentration the migration of Fe^{3+} ions from tetrahedral to the octahedral may not be affected. However, on increasing the substitution, $x>0.4$, the additional Zr^{4+} and Cu^{2+} ions may occupy the tetrahedral (A) sites and force some of the remaining Fe^{3+} ions at A sites to migrate gradually to B sites. As a result, the resistivity is expected to decrease. The Zr–Mn substituted strontium hexaferrite i.e. $SrZr_xM_xFe_{12-2x}O_{19}$ samples synthesized by the sol–gel combustion method [24] showed semiconductors behavior throughout the studied temperature range 300–675 K and does not show the metal–semiconductor transitions.

The energy of activation (ΔE) is calculated from the slope of the linear plots of ln ρ versus reciprocal of the temperature in the semiconducting region. The values of ΔE for the samples are listed in Table 2. The variation in ΔE corresponds to the variation of resistivity viz. the sample of high resistivity also has higher energy of activation and vice versa.

The drift mobility (μ_d) has been calculated using the relation [31];

$$\mu_d = \frac{1}{ne\rho} \tag{5}$$

where e is the charge of electron; ρ, the electrical resistivity and n is the concentration of charge carriers that can be calculated from the relation

$$n = \frac{N\rho_m p_{Fe}}{M} \tag{6}$$

where N is the Avogadro's number; ρ_m, the bulk density; M, the molar mass of the sample; and p_{Fe} is the number of iron atom in the chemical formula of the samples. The drift mobility decreases with temperature in the metallic region $T<T_{M-S}$, but its value increases with increase in temperature in the semiconductor region $T>T_{M-S}$ due to hopping of the charge carriers from one site to another above T_{M-S}. It is evident from Table 2 that drift mobility decreases in samples with $x\geq 0.4$ possibly due to an increase in resistivity in this concentration range.

3.4. Dielectric properties

Dielectric constant (ε') is calculated by the following equation

$$\varepsilon' = \frac{Cd}{\varepsilon_0 A} \tag{7}$$

where C is the capacitance of the pellet in Farad; d, the thickness of the pellet in meter; A, the cross-sectional area of the flat surface of the pellet; and ε_0 is the permittivity constant of free space. The variation of the dielectric constant and the dielectric loss factor ($\tan\delta$) as a function of frequency are shown in Figs. 6 and 7. Both ε' and $\tan\delta$ decrease with increasing frequency. This behavior is normal for ferrites and is believed to be due to the interfacial

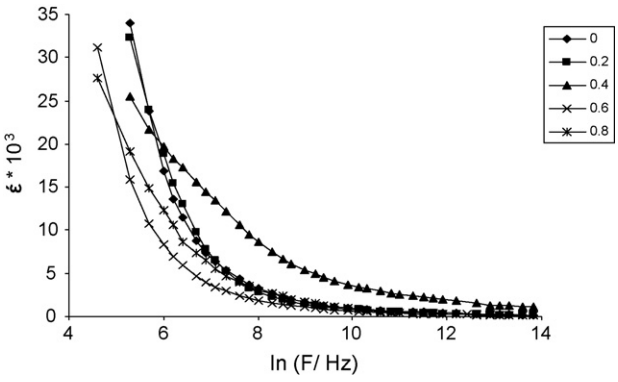

Fig. 6. Dielectric constant (ε') as a function of logarithm of frequency, F, for different $SrZr_xCu_xFe_{12-2x}O_{19}$ ($x=0.0$–0.8) hexaferrite samples.

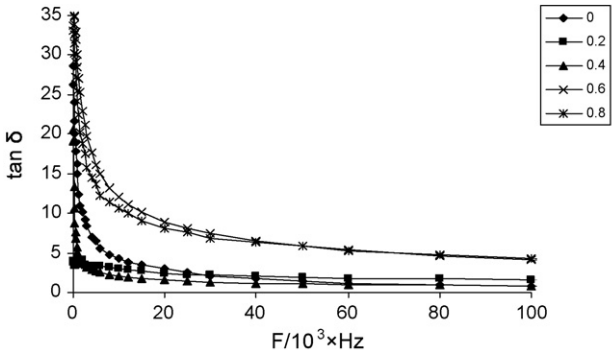

Fig. 7. The dielectric loss factor (tan δ) as a function of frequency for $SrZr_xCu_xFe_{12-2x}O_{19}$ ($x = 0.0$–0.8) hexaferrite samples.

polarization as predicted by Maxwell–Wagner [32]. According to this model, the dielectric structure of ferrites is assumed to be made up of two layers. First layer, being a conducting layer, consists of large number of grains and the other layer consists of grain boundaries that are poor conductors. The polarization in ferrites is via a mechanism similar to the conduction process i.e. by electron exchange between Fe^{2+} and Fe^{3+}. The decrease in polarization with frequency is due to increase in the frequency of externally applied electric field and as a result the electron exchange between Fe^{3+} and Fe^{2+} ions cannot follow the alternating field. The higher values of dielectric constant at low frequency are due to voids, dislocations and other defects [33]. High dielectric constant decreases the penetration depth of the electromagnetic waves by increasing the skin effect. Hence, the much lower dielectric constants obtained for the ferrites warrant their application at high frequency.

The compositional dependence of dielectric constant at frequencies, 0.4, 0.6 and 1 MHz is shown in Table 2. The value of ε' decreases with an increase in Zr–Cu contents for $x \leq 0.4$ and increases with further increase in $x > 0.4$ due to reduction of Fe^{2+} ions at the octahedral sites. The behavior of ε' and tan δ with composition can be explained on the basis of an assumption that the mechanism of the dielectric polarization is similar to the electrical conduction. The dielectric data have an excellent agreement with the resistivity data.

4. Conclusion

A simple and economical route has been presented for producing highly homogeneous Zr–Cu substituted strontium hexaferrite nanoparticles by the co-precipitation method. Substitution of Zr–Cu causes appreciable changes in the structural and electrical properties of the strontium hexaferrite. $SrFe_{12}O_{19}$ is a semiconductor in temperature range 300–675 K however on substitution of Zr_xCu_x ($x = 0.2$–0.8) the sample resistivity reaches a maximum value at the temperature, $T_{M–S}$, defined as metal-semiconductor transition temperature. The $T_{M–S}$ increases with the addition of the dopants up to $x \leq 0.4$. The XRD patterns reveal a single-phase hexagonal structure for the synthesized materials. The crystallite sizes estimated by the Scherrer formula were in the range 26–37 nm as compared to 30–60 and 40–80 nm calculated by TEM and SEM, respectively. The Curie temperature decreases with the increase in Zr–Cu concentration. The drift mobility, dielectric constant and dielectric loss factor decrease while the DC electrical resistivity and activation energy increase for the samples $x \leq 0.4$.

Acknowledgements

The financial support for this work by Higher Education Commission of Pakistan (HEC) is gratefully acknowledged. The authors are grateful to Mr. Iftikhar Gul, Department of Physics of Quaid-i-Azam University, Islamabad for his help in measurements of AC susceptibility and dielectric properties.

Appendix A. Supplementary data

Supplementary data associated with this article can be found, in the online version, at doi:10.1016/j.cej.2007.05.046.

References

[1] S. Singhal, A.N. Garg, K. Chandra, Evolution of the magnetic properties during the thermal treatment of nanosize $BaMFe_{11}O_{19}$ (M = Fe, Co, Ni and Al) obtained through aerosol route, J. Magn. Magn. Mater. 285 (2005) 193–198.
[2] M. Stefanescu, C. Caizer, M. Stoia, O. Stefanescu, Ultrafine, perfectly spherical Ni–Zn ferrite nanoparticles, with ultranarrow distribution, isolated in a silica matrix, prepared by a novel synthesis method in the liquid phase, Acta Mater. 54 (2006) 1249–1256.
[3] J.F. Hochepied, M.P. Pileni, Magnetic properties of mixed cobalt–zinc ferrite nanoparticles, J. Appl. Phys. 87 (2000) 2472–2478.
[4] N. Dishovske, A. Petkov, I. Nedkov, I. Razkazov, Hexaferrite contribution to microwave absorbers characteristics, IEEE Trans. Magn. 30 (1994) 969–971.
[5] B.T. Shrik, W.R. Buessem, Temperature dependence of M_s and K_1 of $BaFe_{12}O_{19}$ and $SrFe_{12}O_{19}$ single crystals, J. Appl. Phys. 40 (1969) 1294–1296.
[6] M. Radwan, M.M. Rashad, M.M. Hessien, Synthesis and characterization of hexaferrite nanoparticles, J. Mater. Process. Technol. 181 (2007) 106–109.
[7] W. Zhong, W. Ding, N. Zhang, J. Hong, Q. Yan, Y. Du, Key step in synthesis of ultrafine $BaFe_{12}O_{19}$ by sol–gel technique, J. Magn. Magn. Mater. 168 (1997) 196–202.
[8] T.G. Carreno, M.P. Morales, C.J. Serna, Barium ferrite nanoparticles prepared directly by aerosol pyrolysis, Mater. Lett. 43 (2000) 97–101.
[9] L. Rezlescu, E. Rezlescu, P.D. Popa, N. Rezlescu, fine barium hexaferrite powder prepared by crystallization of glass, J. Magn. Magn. Mater. 193 (1999) 288–290.
[10] J. Fang, J. Wang, L. Gan, S. Ng, J. Ding, X. Liu, Fine strontium ferrite powders from an ethanol-based microemulsion, J. Amer. Ceram. Soc. 83 (2000) 1049–1055.
[11] K.V.P.M. Shafi, A. Gedanken, Sonochemical approach to the preparation of barium hexaferrite nanoparticles, Nanostrucutred Mater. 12 (1999) 29–34.
[12] J.F. Wang, C.B. Ponton, I.R. Harris, A study of La-substituted strontium hexaferrite by hydrothermal synthesis, J. Alloy Compd. 369 (2004) 170–177.
[13] F. Leccabue, O.A. Muzio, M.S.E. Kany, G. Calestani, G. Albanese, Magnetic properties and phase formation of $SrMn_2Fe_{16}O_{27}$ ($SrMn_2$-W) hexaferrite prepared by the coprecipitation method, J. Magn. Magn. Mater. 68 (1987) 201–212.
[14] Q.Q. Fang, H. Cheng, K. Huang, J. Wang, R. Li, Y. Jiao, doping effect on crystal structure and magnetic properties of chromium-substituted strontium hexaferrite nanoparticles, J. Magn. Magn. Mater. 294 (2005) 281–286.
[15] N. Shirtcliffe, S. Thompson, E.S.O. Keefe, S. Appleton, C.C. Perry, Highly aluminium doped barium and strontium ferrite nanoparticles prepared

by citrate auto-combustion synthesis, Mater. Res. Bull. 42 (2007) 281–287.
[16] S. Thompson, N. Shirtcliffe, E.S.O. Keefe, S. Appleton, C.C. Perry, Synthesis of $SrCo_xTi_xFe_{12-2x}O_{19}$ through sol–gel auto-ignition and its characterization, J. Magn. Magn. Mater. 292 (2005) 100–107.
[17] Q.Q. Fang, H. Bao, D. Fang, J. Wang, Temperature dependence of magnetic properties of zinc and niobium doped strontium hexaferrite nanoparticles, J. Appl. Phys. 95 (2004) 6360–6363.
[18] H. Takaoka, H. Suito, Substitution of Co^{2+} and/or Ti^{4+} ions in strontium hexaferrite grown from Sro-Fe_2O_3-B_2O_3 melts, J. Cryst. Growth 137 (1994) 493–498.
[19] G.K. Thompson, B.J. Evans, Order-disorder and magnetic exchange interactions in substituted strontium hexaferrite $SrA_xFe_{12-x}O_{19}$ (A = Ga, In), J. Appl. Phys. 75 (1994) 6643–6645.
[20] P. Shepherd, K.K. Mallick, R.J. Green, Magnetic and structural properties of M-type barium hexaferrite prepared by co-precipitation method, J. Magn. Magn. Mater. 311 (2007) 683–692.
[21] X. Wang, L. Li, S. Su, Z. Gui, Z. Yue, Low-temperature sintering and high frequency properties of Cu-modified Co_2Z hexaferrite, J. Eur. Ceram. Soc. 23 (2003) 715–720.
[22] A. Mali, A. Ataie, Structural characterization of nano-crystalline $BaFe_{12}O_{19}$ powders synthesized by sol–gel combustion route, Scripta Mater. 53 (2005) 1065–1070.
[23] C. Surig, K.A. Hempel, D. Bonnenbrog, Hexaferrite particles prepared by sol–gel technique, IEEE Trans. Magn. 30 (1994) 4092–4094.
[24] M.J. Iqbal, M.N. Ashiq, comparative studies of $SrZr_xMn_xFe_{12-2x}O_{19}$ nanoparticles synthesized by co-precipitation and sol–gel combustion methods, Scripta Mater. 56 (2007) 145–148.
[25] M.J. Iqbal, F. Saima, Effect of doping of divalent and trivalent metal ions on the structural and electrical properties of magnesium aluminate, J. Mater. Sci. Eng. B 136 (2007) 140–147.
[26] V. Jancarik, M. Papanova, A. Gruskova, D. Kevicka, J. Slama, Determination of magnetocrystalline structure of substituted iron oxides, J. Elec. Eng. 55 (2004) 116–119.
[27] U.V. Chhaya, R.G. Kulkarni, Metal-insulator type transition in aluminium and chromium co-substituted nickel ferrites, Mater. Lett. 39 (1999) 91–96.
[28] N. Rezlescu, E. Rezlescu, Abnormal dielectric behaviour of copper containing ferrites, Solid State Commun. 14 (1974) 69–72.
[29] H. Zhang, J. Zhou, Y. Wang, L. Li, Z. Yue, Z. Gui, Dielectric characteristics of novel Z-type planar hexaferrite with Cu modification, Mater. Lett. 55 (2002) 351–355.
[30] A. Gruskova, J. Lipka, M. Papanova, D. Kevicka, A. Gonzales, G. Mendoza, I. Toth, J. Slama, Mössbauer study of microstructure and magnetic properties (Co, Ni)–Zr substituted Ba ferrite particles, Hyperfin Interact. 156–157 (2004) 187–194.
[31] M.U. Islam, I. Ahmad, T. Abbas, M.A. Choudhry, R. Nazmeen, Effect of Cu substitution for Ni on the properties of $NiFe_2O_4$ system, in: Proceedings of the VI International Symposium on Advance Materials, Topi, Pakistan, 1999, pp. 155–158.
[32] K.W. Wagner, Zur theorie der unvollkommenen dielektrika, Ann. Phys. 345 (1913) 817–855.
[33] L. Sirdeshmukh, K.K. Kumar, S.B. Laxman, A.R. Krishna, G. Sathaiah, dielectric properties and electrical conduction in yttrium garnet (YIG) Bull, Mater. Sci. 21 (1998) 219–226.